Chapter 4
Young type interference oscillations

4.1 Introduction

Electron emission from a homonuclear diatomic molecule due to ionization by an electron, photon or heavy ion can give rise to one of the important quantum mechanical aspect, the Young type electron interference effect. Different experimental and theoretical investigations were carried out in this direction for the simplest diatomic molecule H_2 [9, 10] as already discussed in chapter 1. Further, investigations were extended to more complex diatomic molecules. For N_2 and CO, interference patterns were measured in the photoelectron spectra of the core electrons [85, 86, 87, 88, 89]. Canton *et. al.* showed the observation of Young type interference patterns in the vibrationally resolved valence shell photoionization spectra of H_2, N_2 and CO [90]. Similarly, Ilchen *et. al.* demonstrated the existence of interference oscillations in photoionization of $1\sigma_g$ and $1\sigma_u$ orbitals of N_2 molecule, however the oscillations were out of phase for these two individual orbitals [28]. Chaluvadi et. al. [91] have shown interference oscillaions from the triple differential cross section for electron impact on nitrogen in $3\sigma_g$ orbital. Measurements were also performed to look for interference oscillations in case of ion impact ionization of N_2 and O_2. Baran *et.al.* [25, 92] have reported the evidence of higher order scattering process without signature of primary oscillations in case of MeV energy proton impact on N_2. Similarly Winkworth *et. al.* [93, 94] performed the study for single ionization of O_2 in collision with protons and $O^{5,8+}$ ions and here too higher order oscillations were reported with supression of primary interference oscillations. However, for MeV energy bare C ions impacting on N_2 and O_2 reported in [26, 95, 96], the results showed negligible or no oscillatory structures. Thus there is an ambiguity in the observation of interference oscillations in case of heavy ion impact on N_2 and O_2, unlike for H_2 where oscillations were revealed for all projectiles and second order processes were reported along with the presence of primary oscillations [24, 23]. Such a discrepancy in observing interference oscillations for H_2 but not for N_2 and O_2 when collided with heavy ions was explained theoretically using the CDW-EIS model [27]. In [27] the authors have shown theoretically that for proton impact ionization of N_2, oscillations are visible in individual orbitals, which are phase shifted from each other. Thus while looking for interference oscillations from the DDCS spectra, the contributions from all the orbitals are added up which results in observation of negligible or no oscillations. This theoretical explanation was in accordance to the experimental results of [26, 96]. as well as the out of phase oscillations observed for photoionization of N_2 [28].

Fast electrons being a much gentler probe compared to heavy ions impart much weaker perturbation to the target during collision. Heavy ions can cause simultaneous multiple ionization of outer shells of atoms along with single ionization. Multiple ionization of different orbitals complicates the process, which may lead to non-observation of interference oscillations. Fast electrons possess much lesser probability of multiple ionization compared to that for heavy ion collisions [97]. In this chapter we present the DDCS spectra of the secondary electrons ejected due to the collision of fast electrons with N_2 and O_2 and further investigate for the evidence of interference oscillations in these two multi-electronic homonuclear diatomic molecules.

4.2 Experimental details

Briefly, the experiments were performed using a commercially available Kimball electron gun capable of producing electrons having energies between 1 and 10 keV. For the present set of experiments the electron beam was tuned at 7 keV, i.e., the projectile velocity (v_p) was $\sim$ 22.7 a.u. The O_2 and N_2 target gases were injected into the high vacuum scattering chamber where collision took place with the projectile electrons. For either experiments, the interaction chamber was flooded with the target gases at an absolute pressure of 0.15 mTorr. The ionized electrons were energy analyzed by the hemispherical electrostatic energy analyzer. For N_2 the electrons with energies 1 to 550 eV were detected whereas for O_2 target, the measurements were performed upto 600 eV. The error due to statistical fluctuations were $\sim$ 3 to 5% except for the highest energies at the extreme backward angles, where it went upto 10%. In the next section we will discuss about the results obtained from ionization of N_2 which will be followed by that for O_2 in the successive section.

4.3 Ionization of N_2

4.3.1 Distribution of Electron DDCS at Fixed Emission Angles

Figure 4.1 display the absolute DDCS of the electrons emitted from N_2 when collided with 7 keV electrons. The DDCS are plotted as a function of emitted electron energy for eight different emission angles. It is seen that the cross section decreases over four orders of magnitude in the measured electron energy range. The cross section reaches a maximum in the low energy part of the spectrum due to the contribution from the soft electron emission process. In this region the momentum transfer is small and the electrons are emitted with very large impact parameter. The solid and dashed lines seen in the figure correspond to the theoretical cross sections for N_2 and 2N which were calculated using two different effective charges. For N_2 molecules, the e-DDCS for ionization were calculated in the framework of the complete neglect of differential overlap (CNDO) approximation [98, 99]. Here the molecular orbitals (MO) are constructed

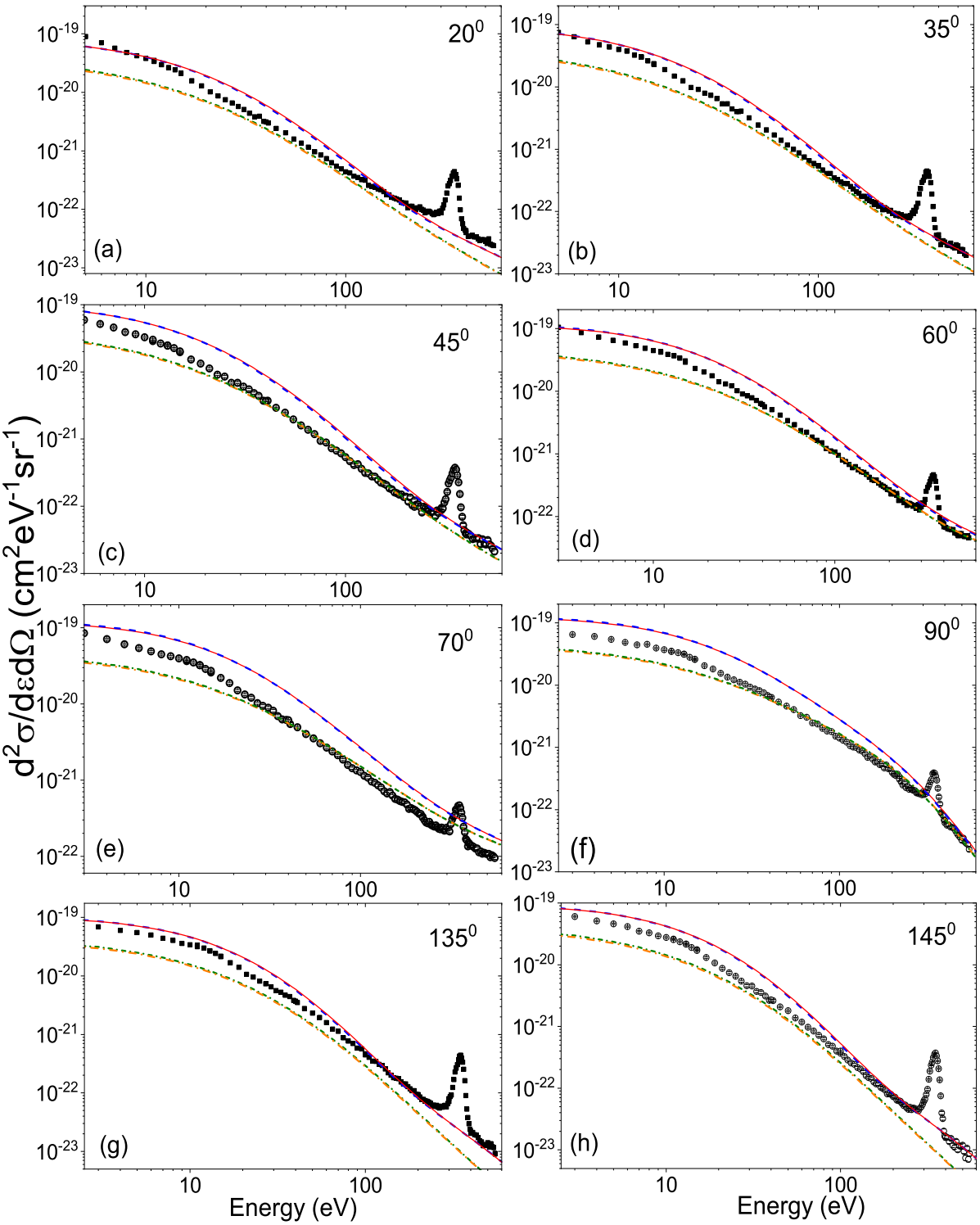

Figure 4.1: Absolute electron DDCS for the collision system 7 keV e^- + N_2, at different emission angles. The red solid line and the blue dashed line represent the calculations for N_2 and 2N, respectively (using Z_T =1). Using Z_T=Z_{bk}, the theoretical cross sections are shown for N_2 (orange dash dotted line) and 2N (green dotted line). For either of the effective charges (Z_T), the calculations for N_2 and 2N are almost identical and cannot be distinguished.

from a linear combination of atomic orbitals in a self-consistent field approach, by using a

minimal basis size, i.e., only the atomic orbitals of those which are occupied in the ground state of the atoms of the molecule are utilized. In this treatment, the weight of such atomic contributions is expressed in terms of the electronic population. The electronic configuration of the ground state of N_2 molecules is (N $1s)^4$ $(\sigma_g 2s)^2$ $(\sigma_u 2s)^2$ $(\pi_u 2p)^4$ $(\sigma_g 2p)^2$. The contribution of the different atomic states to the molecular orbitals extracted from Ref. [100] along with the corresponding measured MO binding energies taken from Ref. [101] are tabulated in Table 4.1. Thus in the monocentric CNDO model, the DDCS for a particular MO reduces to a sum of the cross sections for N atomic compounds weighted by the weights resulting from the Mulliken population analysis for the considered MO (Table 4.1) [99]. The total DDCS for the molecule is obtained as a sum of all MO contributions.

The electronic configuration of the ground state $^4S_{3/2}$ of the N atom is $(1s)^2(2s)^2(2p)^3$. Considering the independent electron model, the multielectronic problem is reduced to a single electron one. It is assumed that one of the target electrons (the *active* electron) is ionized in the final channel of the reaction, whereas the other electrons (the *passive* electrons) remain as frozen in their initial orbitals. Hence, no appreciable relaxation of the target is assumed during the effective collision time. Such an assumption is justified because the effective collision time is much less than the relaxation time of the target at the impact energies of interest [64].

The DDCS for a particular orbital of the N target is obtained from the following expression:

$$\frac{d^2\sigma}{d\Omega_e dE_e} = (2\pi)^4 \frac{k k_s}{k_i} \int d\Omega_s \, |t_{fi}|^2 \tag{4.1}$$

where $\mathbf{k}$ and $\mathbf{k}_s$ are the momenta of the $active$ ejected electron and the scattered one, respectively, whereas $d\Omega_e$ and $d\Omega_s$ represent the corresponding differential solid angles with respect to the incidence direction defined by the incident-electron momentum $\mathbf{k}_i$. $E_e = k^2/2$ is the energy of the emitted electron.

The *prior* version of the transition matrix element is given by

$$t_{fi} = \langle \psi_f^- \mid V_i \mid \psi_i \rangle \tag{4.2}$$

where ψ_i and ψ_f^- are the wavefunctions in the initial channel and the final channel respectively with correct asymptotic conditions. V_i is the perturbation in the entrance channel.

The initial wavefunction is considered as a product between a plane wave for the incident projectile and a bound-state wavefunction ϕ_j for the active electron,

$$\psi_i = \frac{e^{i\mathbf{k}_i.\mathbf{R}}}{(2\pi)^{3/2}} \phi_j(\mathbf{r}) \tag{4.3}$$

where $\mathbf{R}$ and $\mathbf{r}$ are the position vectors of the incident electron and the active electron, respectively. Atomic orbitals ϕ_j $(j = 1s, 2s, 2p)$ are described within the Roothaan-Hartree-Fock approximation [102].

In the first Born approximation, the final-state wavefunction is chosen as,

$$\psi_f^- \cong \frac{e^{i\mathbf{k}_s.\mathbf{R}}}{(2\pi)^{3/2}} C(\mathbf{k},\mathbf{r},\gamma) \tag{4.4}$$

where

$$\begin{aligned} C(\mathbf{k},\mathbf{r},\nu) &= \Gamma(1-i\gamma)\,\frac{e^{i\mathbf{k}.\mathbf{r}}}{(2\pi)^{3/2}} \\ &\times \quad e^{-\pi\gamma/2}\;{}_1F_1[i\gamma;1;-i(kr+\mathbf{k}.\mathbf{r})] \end{aligned} \tag{4.5}$$

describes the ionized electron in the field of the residual target at asymptotically large distances. ${}_1F_1$ is the confluent hypergeometric function and $\gamma = -Z_T/k$ is the corresponding Sommerfeld parameter. Here, Z_T is an effective charge corresponding to the residual target which is seen by the active electron.

According to the choice of the initial state, the perturbation V_i in the initial channel is given by,

$$V_i = \frac{1}{r_p} - \frac{1}{R} \tag{4.6}$$

where $\mathbf{r}_p = \mathbf{r} - \mathbf{R}$ is the position vector of the active electron with respect to the projectile. The perturbation V_i corresponds to the interaction of the projectile with the $active$ electron and with a net charge equal to unity. This is compatible with the complete screened charge of the nuclei by the *passive* electrons.

In order to evaluate the influence of the passive electrons in the final channel, either an asymptotic charge $Z_T = 1$ which corresponds to a total screening of the nucleus, or $Z_T = Z_{bk} = \sqrt{-2n_j^2\epsilon_j}$ [103] are used in the DDCS calculations for both N and N_2 targets. In case of the atomic cross section calculations, ϵ_j is the Roothaan-Hartree-Fock energy [102], whereas for N_2 computations, ϵ_j represents the MO energies shown in Table 4.1. In either cases, n_j is the principal quantum number of the atomic orbital involved in the calculations.

Table 4.1: Population and experimental binding energies of the N_2 molecular orbitals (MO).

MO	Population [100]	Exp. Energy (eV) [101]
N $1s$	4.00 N $1s$	-409.90
$\sigma_g 2s$	1.50 N $2s$ + 0.50 N $2p$	-37.23
$\sigma_u 2s$	1.47 N $2s$ + 0.53 N $2p$	-18.60
$\pi_u 2p$	4.00 N $2p$	-16.80
$\sigma_g 2p$	0.5 N $2s$ +1.50 N $2p$	-15.50

The calculations for N_2 and 2N are seen (Figure 4.1) to merge almost completely for either values of Z_T. The DDCS with Z_T=1 agrees with the experimental data qualitatively, but

quantitatively overestimates them for all the emission angles. On the other hand, the calculation corresponding to Z_{bk} are seen to have better agreement with the data beyond 20 eV for all angles. In case of higher backward angles, the DDCS with Z_T=Z_{bk} underestimates the data. For the low energy electrons, the discrepancy between data and theoretical calculation using Z_{bk} is larger for the forward angles compared to the backward angles. The sharp peak observed at about 355 eV, corresponds to the K-LL Auger electron emission due to the presence of an inner shell vacancy.

4.3.2 Theoretical understanding of interference effect from diatomic molecule

In case of electron scattering from two nucleon centres, using the prescription of Messiah [104], the cross section for electron emission from a homonuclear diatomic molecule (e.g. N_2) can be written as

$$\frac{d^3\sigma_{N_2}}{dqd\Omega d\epsilon} = \frac{d^3\sigma_{2N}}{dqd\Omega d\epsilon}[1 + cos(p \cdot d)]. \tag{4.7}$$

where the solid angle element $d\epsilon$ and $d\Omega$ are associated with the outgoing electron. d is the inter-nuclear distance of the N_2 molecule (d = 2.1 a.u.) and $p = k - q$ is the recoil ion momenta, which is given by the difference between the outgoing electron momenta (k) and the momentum transfer (q). The term inside the square bracket is due to the interference caused by both the N atoms, and $d^3\sigma_{2N}/dqd\epsilon d\Omega$ represents the cross-section from the two N atoms acting as two independent particles. Now, $p \cdot d = pdcos\alpha$ where α denotes the angle between the molecular orientation and the recoil ion. Since, recoil ions were not detected, one can average over all possible molecular orientations in space

$$\frac{\int_0^\pi [1 + cos(pdcos\alpha)]2\pi sin\alpha d\alpha}{\int_0^\pi 2\pi sin\alpha d\alpha} = 1 + \frac{sin(pd)}{pd}. \tag{4.8}$$

Inserting this in Equation 4.7, we get

$$\frac{d^3\sigma_{N_2}}{dqd\Omega d\epsilon} = \frac{d^3\sigma_{2N}}{dqd\Omega d\epsilon}\Big[1 + \frac{sin(pd)}{pd}\Big]. \tag{4.9}$$

To obtain the double differential cross sections relevant to the present experiment, an integration over all possible values of q is necessary. According to the pioneering work of Bethe [105], the cross-section can be divided into two parts namely, a dipole part representing the soft collision and the other representing a binary collision or 'head-on' collision between the projectile and the target electron.

$$\frac{d^3\sigma_{N_2}}{dqd\Omega d\epsilon} = \frac{d^3\sigma_{2N}^{dip}}{dqd\Omega d\epsilon}\Big[1 + \frac{sin(\mid k - q \mid d)}{\mid k - q \mid d}\Big] + \frac{d^3\sigma_{2N}^{bin}}{dqd\Omega d\epsilon}\Big[1 + \frac{sin(\mid k - q \mid d)}{\mid k - q \mid d}\Big]. \tag{4.10}$$

The dipole part $(d^3\sigma_{2N}^{dip}/dqd\Omega d\epsilon)$ has a sharp maximum at the minimum momentum transfer given by, $q_{min} = \Delta E/v_p$ where ΔE is the energy transfer and v_p is the projectile velocity. For high velocity projectiles, such as $v_p \sim 23$ a.u., q_{min} is small and hence a peaking approximation is applied where $q_{min} \sim 0$. Considering the first term of the R.H.S of Equation 4.10

$$\int dq \frac{d^3\sigma_{2N}^{dip}}{dqd\Omega d\epsilon}\Big[1 + \frac{sin(\mid k-q \mid d)}{\mid k-q \mid d}\Big] \simeq \frac{d^2\sigma_{2N}^{dip}}{d\Omega d\epsilon}\Big[1 + \frac{sin(\mid k-q_{min} \mid d)}{\mid k-q_{min} \mid d}\Big]. \tag{4.11}$$

Setting $q_{min} \sim 0$ in Equation 4.11 we get

$$\int dq \frac{d^3\sigma_{2N}^{dip}}{dqd\Omega d\epsilon}\Big[1 + \frac{sin(\mid k-q \mid d)}{\mid k-q \mid d}\Big] \simeq \frac{d^2\sigma_{2N}^{dip}}{d\Omega d\epsilon}\Big[1 + \frac{sin(kd)}{kd}\Big]. \tag{4.12}$$

A peaking approximation can also be applied to the binary part of the cross section in Equation 4.10 by setting $p = \mid k-q \mid d = p_i$ where p_i is the mean initial momentum of the bound electron [106]. With these assumptions Equation 4.10 becomes

$$\frac{d^2\sigma_{N_2}}{d\Omega d\epsilon} = \frac{d^2\sigma_{2N}^{d}ip}{d\Omega d\epsilon}\Big[1 + \frac{sin(kd)}{kd}\Big] + \frac{d^2\sigma_{2N}^{b}in}{d\Omega d\epsilon}\Big[1 + \frac{sin(p_id)}{p_id}\Big]. \tag{4.13}$$

For all practical purposes, p_i can be taken close to unity, so that only the dipole term is responsible for bearing the signature of two-center interference in the electron emission spectra of di-atomic molecules [106]. A closer look at Equation 4.13 reveals that the oscillations doesn't have any angular dependence. This is because the integration over all possible molecular orientation in Equation 4.8 reserves the essential features of the interference in the electron emission spectra but, it cancels the dependence of the interference term on the electron emission angle θ. It was later noted by Nagy *et. al.* [107], that the integration over the momentum transfer q leaves behind the angular dependence through the parallel component of the momentum transfer, which in turn is related to the parallel component of the outgoing electron's momentum $k_\parallel = kcos\theta$. Taking this into account, Nagy *et. al.* derived an expression for the DDCS spectra given by :

$$\frac{d^2\sigma_{N_2}}{d\Omega d\epsilon} = \frac{d^2\sigma_{2N}}{d\Omega d\epsilon}\Big[1 + \frac{sin(k_\parallel d)}{k_\parallel d}\Big]. \tag{4.14}$$

According to this expression the phase of the oscillation should be identical in a forward emission angle θ and its complementary backward emission angle $\pi - \theta$. However, it was shown by Misra *et. al.* [16] that the frequency of oscillation at an angle θ may be different to its complementary counterpart at $\pi - \theta$. Thus Equation 4.14 was further modified as follows :

$$\frac{d^2\sigma_{N_2}}{d\Omega d\epsilon} = \frac{d^2\sigma_{2N}}{d\Omega d\epsilon}\Big[1 + \frac{sin(kc(\theta)d}{kc(\theta)d}\Big]. \tag{4.15}$$

Here, $c(\theta)$ is an adjustable frequency parameter and the term inside bracket is the interfer-

ence term [8, 9, 107]. k represents the electron momentum in a.u. and d is the internuclear distance (2.1 a.u for N_2) as already mentioned above.

4.3.3 Experimental-to-theoretical DDCS ratio

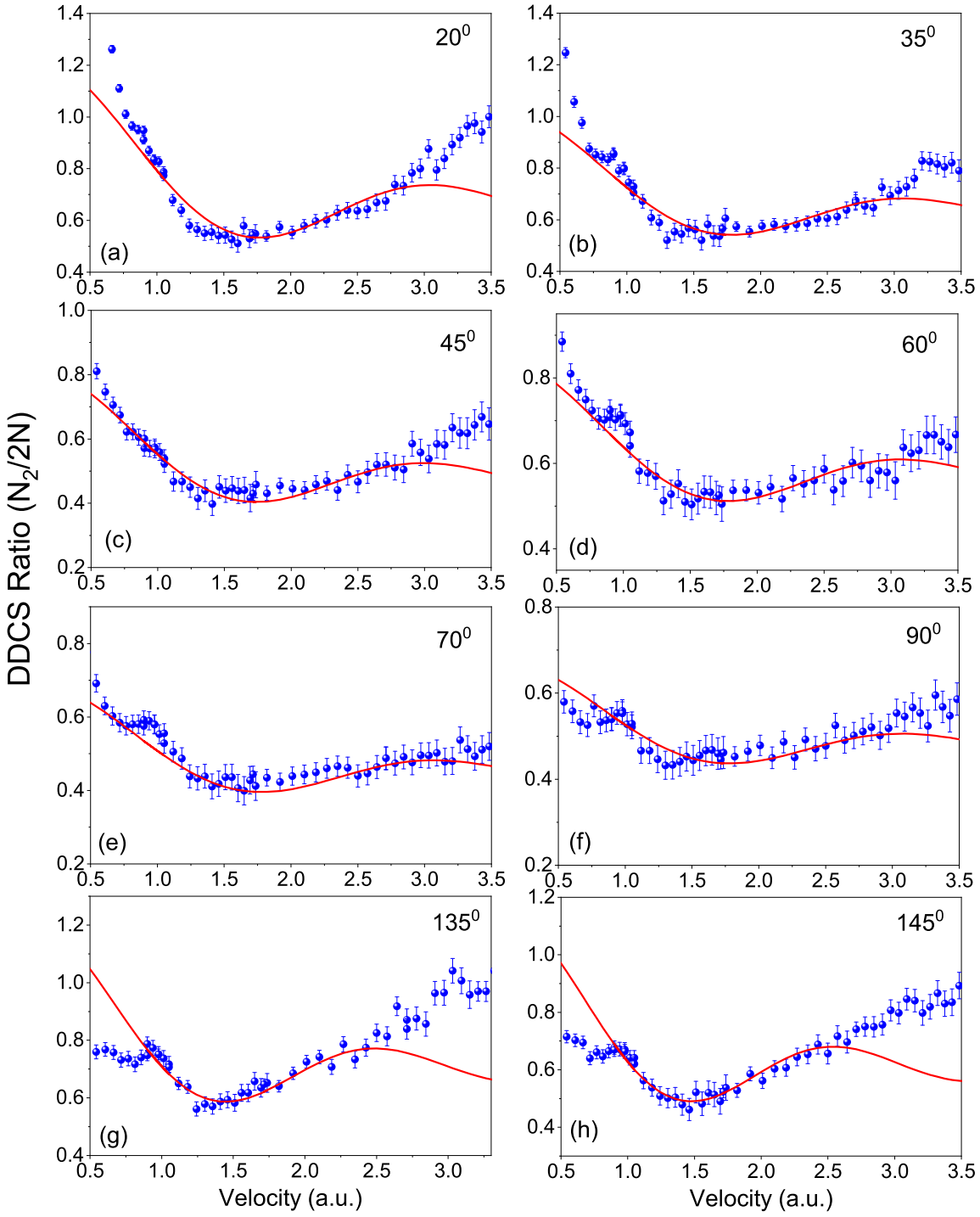

Figure 4.2: Experimental-to-theoretical DDCS ratios ($\frac{d^2\sigma_{N_2}}{d\Omega d\epsilon}/\frac{d^2\sigma_{2N}}{d\Omega d\epsilon}$) at eight different emission angles. Theoretical cross section for 2N using Z_T = 1. Solid line corresponds to the analytical fitting in Equation 4.16.

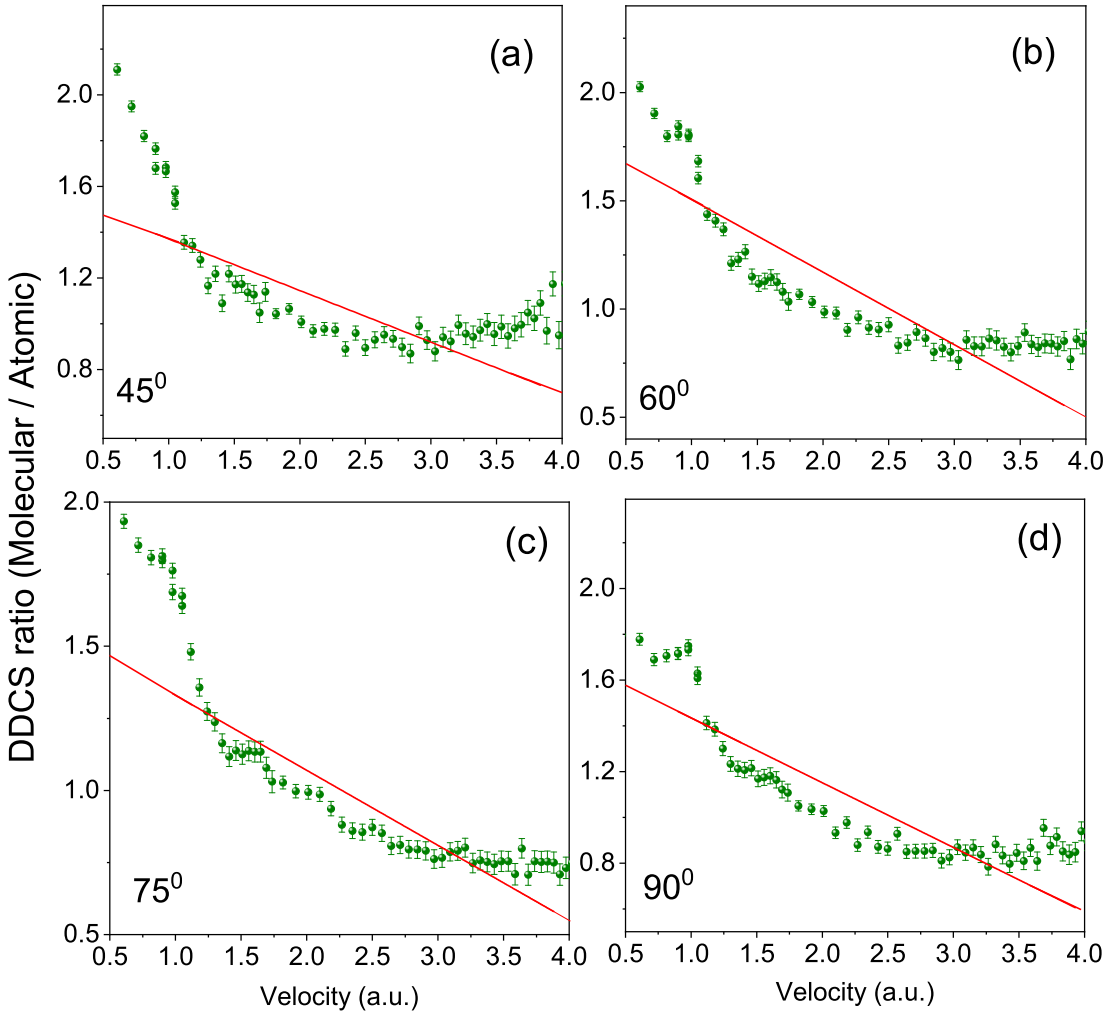

Figure 4.3: DDCS ratios using Z_T=Z_{bk} for atomic N cross section. Solid line shows a linear function of negative slope used for fitting the ratios.

From Figure 4.1 it is seen that the DDCS for N_2 and independent N atoms fall by several orders of magnitude with the electron energy, whereas, as seen from Equation 4.15 the variation due to interference effect is rather small. To enhance the visibility of interference oscillation, it is essential to omit the variation of cross section with electron energy. Thus the ratio DDCS(N_2)/2DDCS(N) is a tool for investigating the interference oscillation. The DDCS for N_2 was divided by the corresponding DDCS of the two N atoms. In the absence of experimental data for atomic nitrogen, the experimental DDCS for N_2 were divided by theoretical DDCS for 2N. The theoretical DDCS for atomic nitrogen ($\frac{d^2\sigma_{2N}}{d\Omega d\epsilon}$) were calculated using the effective charges Z_T=1 and Z_T=Z_{bk}, already discussed in the previous section. Figure 4.2 and Figure 4.3 display the DDCS ratios obtained using Z_T = 1 and Z_T = Z_{bk}, respectively. In Figure 4.2, a half sinusoidal oscillatory structure is observed for all the emission angles. In all the cases, the oscillation is seen about a horizontal line, for 20^0 and 30^0 it is seen about 0.7 and for rest of the angles it is seen around a value of 0.5 whereas for 145^0 oscillation is seen around 0.6. From

Equation 4.15 it is clearly seen that the oscillations are expected to be around a horizontal line near 1.0, but as seen from Figure 4.1, the DDCS calculations for 2N using Z_T=1 are higher than the measured data for N_2 for all the emission angles. This difference between the experimental measurements and the theoretical predictions leads to the oscillations being observed below 1.0. For angles 135^0 and 145^0, the oscillation frequency is seen to be higher compared to the other angles. The ratios are fitted by the Cohen-Fano type function (shown by solid lines in Figure 4.2) given by :

$$\sigma_{norm}(k,\theta) = A + F\frac{sin(kc(\theta)d)}{kc(\theta)d} \tag{4.16}$$

where $\sigma_{norm}(k,\theta)$ represents the DDCS ratio i.e ($\frac{d^2\sigma_{N_2}}{d\Omega d\epsilon}/\frac{d^2\sigma_{2N}}{d\Omega d\epsilon}$). The fitted curve matches quite well with the ratios for most of the emission angles. For 135^0 and 145^0 discrepancy is observed beyond 2.5 a.u. and such a mismatch may be ascribed to the difference between the measured data and theory for 2N.

Figure 4.3 shows similar DDCS ratios which were obtained using the effective charge Z_T=Z_{bk} for 2N. The ratios show an oscillatory structure overriding on a straight line of negative slope. To reveal the oscillations clearly, a linear function (shown by red solid line) was fitted to the ratios for all the emission angles. The cross section ratios were then divided by the fitted line and the resulting DDCS ratios are shown in Figure 4.4 for different forward and backward angles. The linear fitting was performed to look for the oscillation about a horizontal line. From all the eight panels in Figure 4.4 it is clearly observed that half sinusoidal oscillatory structures exist around a horizontal line near 1.0 for all the angles. The interference oscillations observed in Figure 4.4 is qualitatively similar to that observed using Z_T=1, shown in Figure 4.2. The ratios in Figure 4.4 were further fitted by the Cohen-Fano function given in Equation 4.16. The fitted function (shown by red solid lines) agrees well with the experimental-to-theoretical DDCS ratios.

From the above discussions, it is clearly observed that the choice of effective charge Z_T for calculating the atomic N cross sections, play a crucial role in determining the shape of the oscillations in the DDCS ratios (Figure 4.2 and Figure 4.3). Although looking at Figure 4.1 it is observed that the theoretical DDCS for 2N calculated using Z_T=Z_{bk} matches well with the measured DDCS of N_2 at the higher emission energies, but the ratios do not reveal proper oscillation. The oscillation, about a horizontal line, is finally revealed only after dividing by a fitted straight line. On the other hand, the DDCS for 2N calculated using Z_T=1, though overestimates the measured cross sections for N_2 (Figure 4.1), but provides clearer oscillation about a horizontal line.

4.3.4 Frequency Parameter

Figure 4.5 display the variation of the angle dependent frequency parameter $c(\theta)$ as a function of the electron emission angles. The frequency parameter $c(\theta)$ was obtained from the fitting

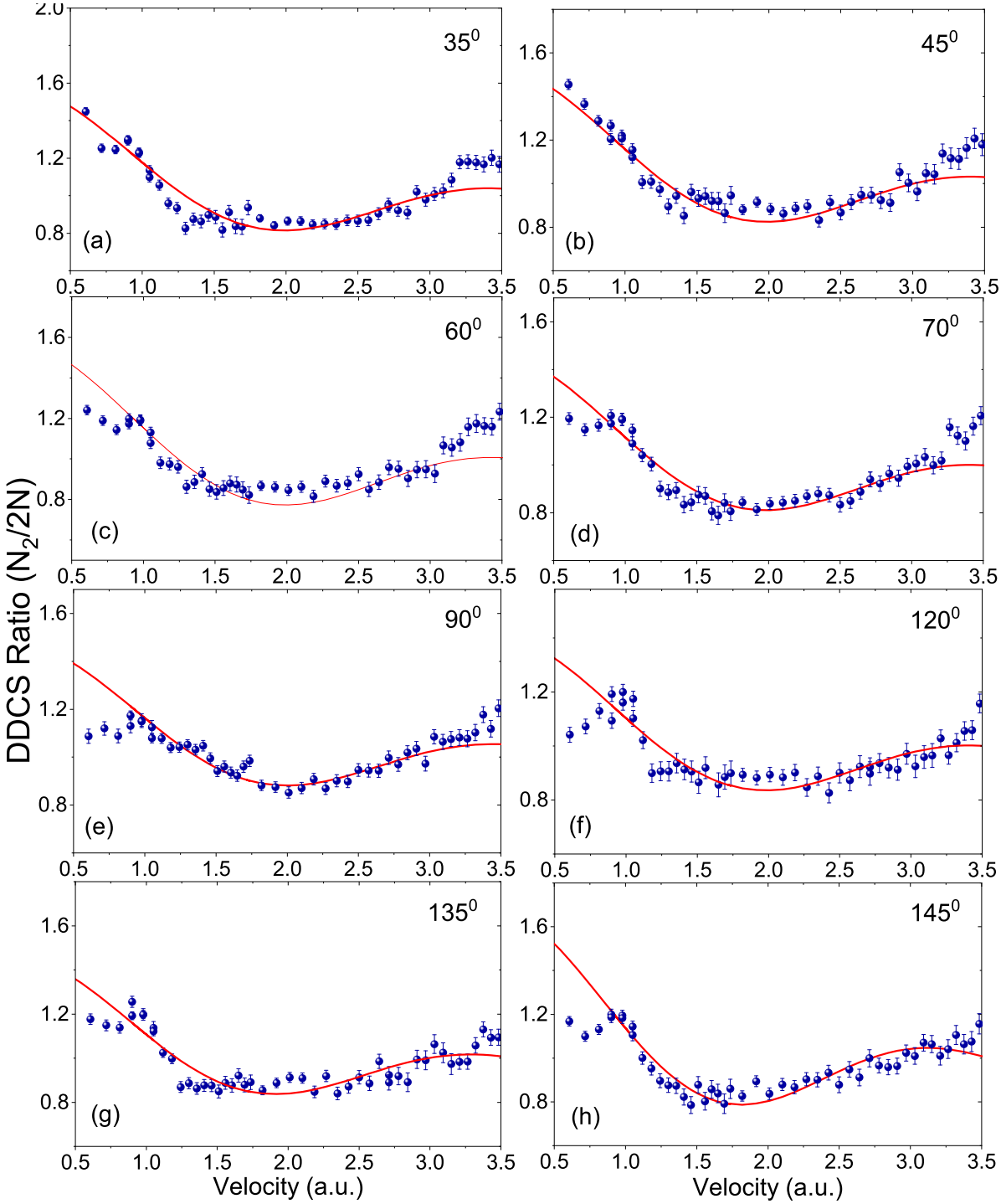

Figure 4.4: DDCS ratios obtained after dividing by the linear fitted line in Figure 4.3. Solid line shows the fitted function in Equation 4.16.

function in Equation 4.15 for all the angles. Figure 4.5(a) shows the $c(\theta)$ values which were obtained by fitting the DDCS ratios where effective charge Z_T = 1 was used for calculating the cross section for atomic nitrogen. Similarly in Figure 4.5(b), the $c(\theta)$ values are plotted for the fitting shown in Figure 4.4 where the DDCS for 2N were calculated using Z_T=Z_{bk}. In Figure 4.5(a), for all the forward angles, the frequency of oscillation remains almost constant

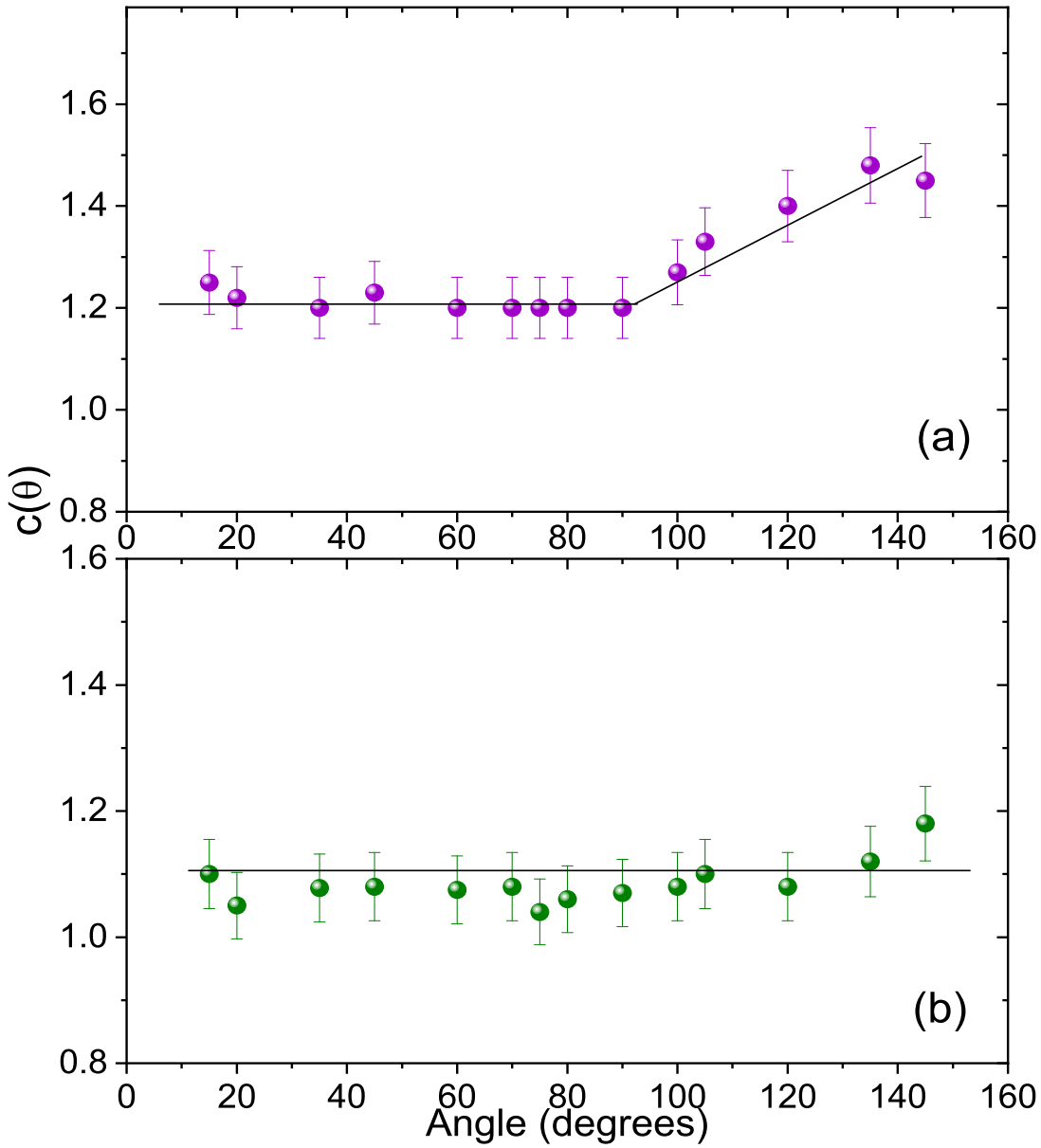

Figure 4.5: Frequency parameter $c(\theta)$ plotted as a function of emission angles. Black solid line : guide to eye.

upto 90^0. However, with further increase in the emission angles, i.e., for the backward angles, the frequency parameter increases steadily with the observation angle. The frequency parameter changes from a value of 1.2 to 1.45 over the entire angular range showing an enhancement of a factor of about 1.20(8). However, in Figure 4.5(b) an almost flat distribution is obtained for $c(\theta)$ for all the emission angles, except for 145^0 where the frequency parameter is higher. The black solid lines in both the panels are shown as guide to eye. It may be mentioned that the shape of the angular dependence of $c(\theta)$ for N_2 is quite different to that for H_2 [108]. This shape is widely dependent on the effective charge considered for the theoretical calculations for atomic target, as can be readily observed from the two panels in Figure 4.5. The flat distribution in Figure 4.5(b) might be due to the fact that in this case the $c(\theta)$ values were not directly

obtained from the DDCS ratios, rather the fitting had to be done after diving the DDCS ratios by the linear fitting to reveal the oscillations clearly. It is inferred that the choice of Z_T=Z_{bk} for calculating DDCS for atomic N may not be the right option for investigating the interference oscillations.

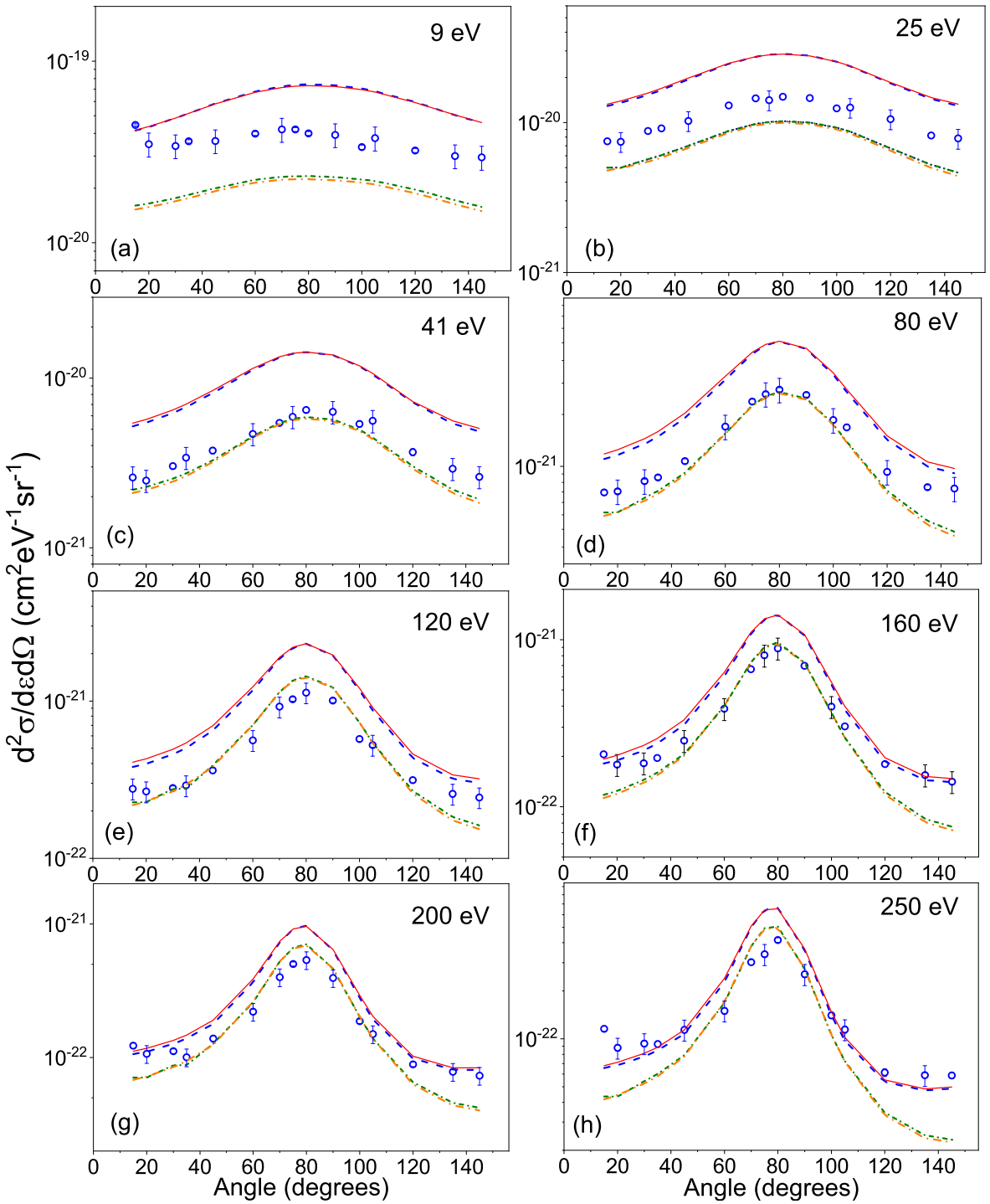

Figure 4.6: Absolute electron DDCS at different emission energies, collision system : 7 keV e^- + N_2. Legends are similar to those in Figure 4.1.

4.3.5 Distribution of Electron DDCS at Fixed Emission Energies

In Figure 4.6 the angular distribution of DDCS have been shown for different electron emission energies. The absolute error bars are shown for some data points. For low emission energies, the distributions are almost flat representing the soft collision mechanism. With the increase in electron emission energy, the distributions gradually show a peaking structure around 80^0. This peaking structure is due to the binary nature of collisions and the peak gets sharper with increase in emission energy. Details on the binary collisions is provided in chapter 6. The four theoretical curves seen in each panel correspond to the DDCS calculated for N_2 and 2N with the effective charge Z_T = 1 and Z_T = Z_{bk}. Overall a qualitative agreement is seen between the experimental measurements and the theoretical calculations in all cases. Quantitatively, the DDCS predicted using Z_T = 1 overestimates the measured data. The calculations with Z_{bk} underestimate the data for 9 eV and 25 eV, but with increase in emission energies, the agreement is better. A closer inspection into the plots show that the curves for Z_T=Z_{bk} are below the measured values for extreme forward and backward angles, with the discrepancy being largest for 250 eV. All the four theoretical curves reproduce the soft collision mechanism and the head on collisions properly. It is further noticed, both experimentally and theoretically, that the cross sections at extreme forward angles are slightly higher than the DDCS at extreme backward angles. This indicates a minor signature of forward-backward angular asymmetry in case of electron impact collisions.

4.3.6 Asymmetry Parameter

From the angular distribution spectra of electron emission, it is observed that the cross section in the forward angles are higher than that in the backward angles. Such an increase in the electron yield in the forward direction compared to its complementary backward angle produces an asymmetry in the angular distribution of the DDCS spectra. This difference in the angular distribution is explained in terms of the angular asymmetry parameter. Such an asymmetry is caused due to the two center effect (i.e., when the ejected electron is under the influence of the projectile and the target ion in the final state) and the non-Coulombic potential of multi-electronic target [109]. In case of highly charged ion impact on atoms or molecules, two center effect plays a major role to explain the angular asymmetry along with the non-Coulombic nature of the target potential, however, for electron impact ionization studies, the departure from the Coulombic potential is the main reason for such asymmetry. The angular asymmetry parameter $\alpha(k)$ is defined as follows :

$$\alpha(k,\theta) = \frac{\sigma(k,\theta) - \sigma(k,\pi-\theta)}{\sigma(k,\theta) + \sigma(k,\pi-\theta)}. \tag{4.17}$$

where the electron energy $\epsilon_k = \frac{k^2}{2}$ in a.u. and θ is an extreme forward angle. Expanding the

DDCS ($\sigma(k,\theta)$) in terms of the Legendre polynomials, one gets :

$$\sigma(k,\theta) = \frac{d^2\sigma}{d\epsilon_e d\Omega_e} = \sum_L \beta_L P_L(cos\theta). \tag{4.18}$$

where β_L is the angular anisotropy parameter, $P_L(cos\theta)$ is the Legendre polynomial and θ is the electron emission angle. According to Fainstein *et. al.* [109], the values upto L=2 contribute mainly to the asymmetry parameter. Thus expanding $\sigma(k,\theta)$ for θ=0 and considering the first few terms of the series expansion, we get $\alpha(k)$ as follows :

$$\alpha(k) = \frac{\sum_j \beta_{2j+1}(k)}{\sum_j \beta_{2j}(k)} \simeq \frac{\beta_1(k)}{\beta_0(k)+\beta_2(k)}. \tag{4.19}$$

Thus $\alpha(k)$ is the ratio of the odd terms to the summation of even terms. As the variation of angular distribution near 0 and π is very small so in most of the cases we have used the measured DDCS for extreme angle (e.g. θ=20^0 or 30^0 or 35^0) to calculate $\alpha(k)$ approximately.

4.3.7 Interference oscillations from forward-backward angular asymmetry

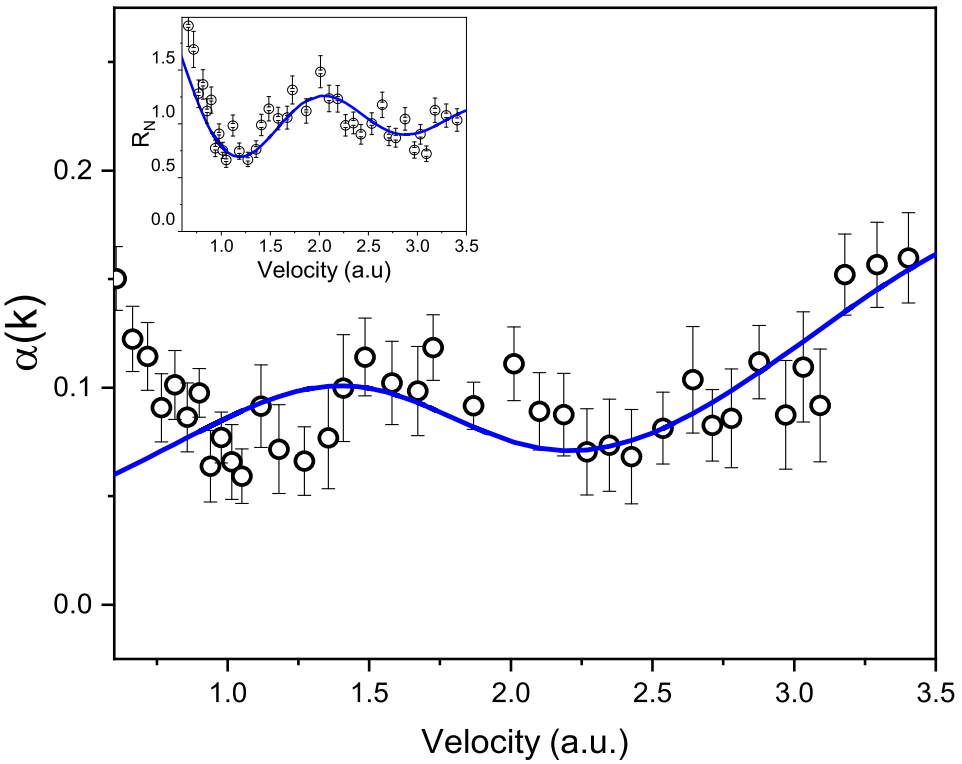

Figure 4.7: Forward-backward asymmetry parameter from measured DDCS for N_2 at 35^0 and 145^0. Solid line shows the model fitting given by Equation 4.20. Inset : Asymmetry parameter divided by the first order model fitting.

The forward-backward angular asymmetry can be used as another tool for investigating the interference oscillations [16]. From Figure 4.2 and Figure 4.3 we have seen that although interference oscillations were clearly observed from the DDCS ratios, but the pattern of oscillation was dependent on the choice of effective charge Z_T used for atomic N calculations. In case of forward-backward angular asymmetry, the presence of oscillations (if any) can be determined directly from the measured DDCS of the molecular target and hence it is free from atomic cross section and the choice of any effective charge. Further, absolute normalization of the DDCS data are also not required. As already discussed in the previous section, in case of electron impact ionization, the non-Coulombic potential for the multi-electronic molecule gives rise to the angular asymmetry between forward and backward angles. For a diatomic molecule, the Young type interference can also influence the asymmetry parameter [16, 110, 22]. The asymmetry parameter, obtained from the experimentally measured DDCS of N_2 for two complementary angles (35^0 and 145^0) is shown in Figure 4.7 as a function of electron velocity. The quantity $\alpha(k)$ shows a full sinusoidal oscillation in the ejected electron velocity range of 0.6 to 3.5 a.u. Such a nice oscillatory structure between low forward angle and its complementary backward angle provides clear indication of the fact that frequency of oscillation varies between forward and backward angles. Further, from Figure 4.5(a) it is also observed that the frequency of oscillations are greater for backward angles compared to forward angles. However Figure 4.5(b) shows slightly different behaviour indicating that the use of Z_T=Z_{bk} may not be the right choice for investigating the interference oscillations. Thus $\alpha(k)$ provides a much clearer picture of the observation of oscillations directly from the experimental measurements, devoid of any atomic cross section and hence no use of effective charge.

Replacing the DDCS in Equation 4.17 by that in Equation 4.15, one gets an expression for the asymmetry parameter $\alpha(k)$ as follows [110] :

$$\alpha(k) = \frac{k\beta c(\theta)d(A-B) + [A\beta sin(kc(\theta)d) - Bsin(k\beta c(\theta)d)]}{k\beta c(\theta)d(A+B) + [A\beta sin(kc(\theta)d) + Bsin(k\beta c(\theta)d)]} \tag{4.20}$$

where, electron energy $\epsilon_k = k^2/2$, A and B are the amplitudes of oscillation for the two complementary angles, d is the internuclear distance, $c(\theta)$ is the frequency of oscillation for low forward angle having θ (=35^0 in this case) and β is the ratio of oscillation frequency for backward to forward angles, i.e. $c(\pi-\theta)/c(\theta)$. The model fitting is seen to match very well to the experimental data above 1.4 a.u, shown by the solid line in Figure 4.7.

4.3.8 Second order interference effect

In addition to first order scattering, there can also be contributions from higher order scattering mechanism [23, 24, 104]. A closer look at Figure 4.7 shows that although the fitting matches well with the data but a periodic deviation is observed below 1.4 a.u. Such a deviation indicates the presence of second order scattering effects which will generate a higher frequency component in oscillation. This effect occurs when a particle after getting scattered from one center

moves towards the second center and finally gets scattered off the second center. Thus an additional path length is introduced, generating higher oscillation frequency. In order to understand this higher order effect, the data points were divided by the first order fitting function (shown in the inset in Figure 4.7). The resulting data reveals an oscillatory structure which is further fitted by a model (solid-line), similar to the Cohen-Fano type formalism :

$$R_N = D + E\frac{sin(nkd)}{nkd}. \tag{4.21}$$

Here n is the frequency of oscillation, which is found to be 1.8, i.e. almost twice the frequency of the primary oscillation. Thus $\alpha(k)$ provided a convincing proof of interference oscillation along with the signature of higher order contribution arising from a second order scattering mechanism.

4.4 Ionization of O_2

In this section and the following sub sections we will be discussing about ionization of O_2 in collisions with 7 keV electrons. The DDCS ratios (experimental/theoretical) for O_2 to that for 2O have been derived from the measured quantities and theoretical predictions. Further the asymmetry between forward and backward angles have been deduced to explore the presence of interference oscillations.

4.4.1 Distribution of Electron DDCS at Fixed Emission Angles

Figure 4.8 display the absolute DDCSs of the secondary electrons emitted from O_2 for eight different electron emission angles. The cross section decreases by four to five orders of magnitude in the scanned secondary electron energy range. The DDCS is maximum at the lowest electron energies. This region is dominated by the soft collision process. Here the momentum transfer from the projectile is very less and hence the electrons are ejected with large impact parameter. The intermediate part of the spectrum is dominated by the two center effect although in case of electrons as probe, two center effect is not a dominant feature compared to highly charged ions. The sharp peak observed at around 480 eV is contributed by the K-LL Auger electrons. Since the peak is sitting over a rapidly falling background, the peak position may vary a bit for different emission angles. However looking at the insets in Figure 4.8 its clear that the peak appears at the expected energy i.e. 480 eV for all the angles. The solid line in each case corresponds to twice the atomic oxygen calculations. For calculating the DDCS for atomic-O, the independent electron model was employed where it is assumed that only one target electron (*active* one) is ionized in the final channel whereas the remaining *passive* electrons are considered as frozen in their initial orbitals during the reaction. The cross sections were calculated within a first-order Born approximation (B1), where the projectile dynamics is described by a plane-wave at both the initial and final channels. In the initial channel, a Roothaan-Hartree-Fock representation

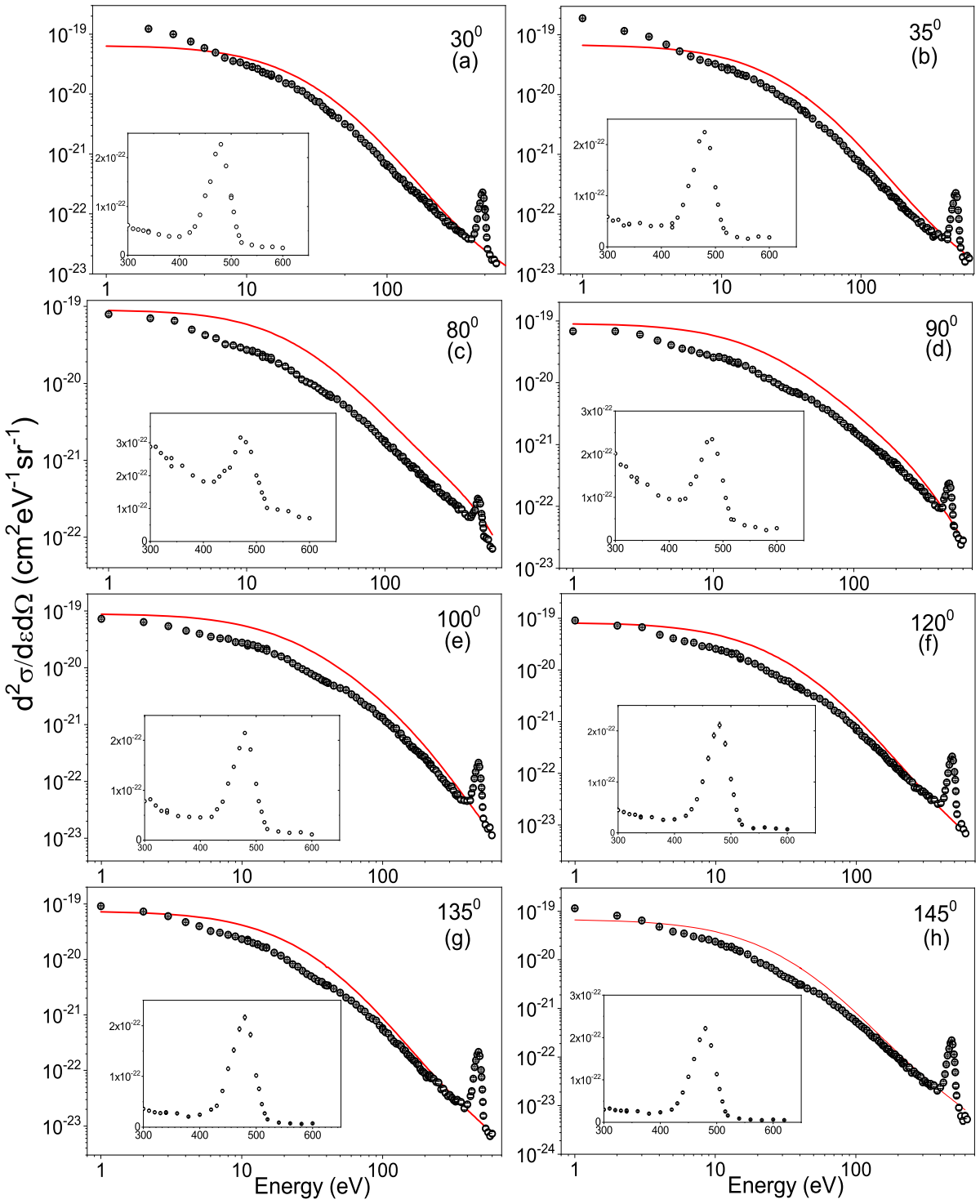

Figure 4.8: Absolute electron DDCS for the collision system 7 keV $e^- + O_2$ shown for different emission angles. The red solid line correspond to the theoretical DDCS for twice of atomic oxygen calculated using $Z_T = 1$.

of the different atomic orbitals was employed [102]. In the final channel, a Coulomb residual continuum function was considered having an effective charge $Z_T = 1$. This charge may be interpreted as the asymptotic charge felt by the ionized electron due to its interaction with

the residual target. Since the theoretical calculations for atomic oxygen are required for exploring the interference patterns from the DDCS ratios so particular attention was devoted for determining the DDCS for atomic target. The calculations show a qualitative agreement with the measured e-DDCS for O_2. Quantitatively, the DDCS for 2O predicts higher cross sections compared to the experimentally obtained DDCS for O_2 particularly for the intermediate angles (80^0, 90^0, 100^0). For the extreme forward and backward angles, the DDCS for 2O are seen to be close to the data points.

4.4.2 Experimental-to-theoretical DDCS ratios

In this section we have derived the ratios between the experimental DDCS for O_2 and the theoretical DDCS for 2O. This is done to check for the contribution due to the interference effect, similar to that seen in case of N_2 target. Using Equation 4.15 and dividing the molecular DDCS by twice the corresponding atomic cross section, we obtain the contribution due to the interference term. In case of O_2, the internuclear distance d = 2.28 a.u. Similar to the case for N_2, due to the difficulty in producing atomic source for these targets, the theoretical DDCS for 2O are used for determining the ratios. Figure 4.9 show the DDCS ratios for oxygen target obtained for several forward and backward angles. The ratios reveal clear oscillatory structures for all the different emission angles. For 30^0 and 35^0, half sinusoidal oscillatory structure is observed about a horizontal line whereas for other angles, full oscillation is observed. Further, it is noticed that the oscillations at the backward angles ride over a straight line of small positive slope. A close look at the ratio plots reveal that the oscillations are around a value of 0.5-0.6, instead of the expected value 1.0. The reason for the oscillations being observed around 0.5 can be easily understood from Figure 4.8, where the DDCS for 2O were higher than that for O_2 and hence dividing the DDCS of O_2 by that of 2O will reduce the absolute values of the ratio below 1.0. Similar results were also obtained for DDCS ratios of nitrogen target. The oscillatory structures were further fitted using Equation 4.16. To account for the minor increasing trend in the oscillations at the backward angles, a linear term was added along with the Cohen-Fano term in Equation 4.16. The slope remained almost same for all the angles. The fitting matched well to the oscillatory structures for almost all the angles, except for 145^0, where deviation was observed beyond 2.8 a.u.

4.4.3 Distribution of Electron DDCS at Fixed Emission Energies

Figure 4.10 displays the measured absolute DDCS of electrons as a function of emission angles for eight different electron energies namely 9 eV, 11 eV, 15 eV, 35 eV, 90 eV, 180 eV, 320 eV and 400 eV. The total error bars are shown for some of the data points. The angular distribution is observed to be almost flat for the low emission energies, explained by the soft collision mechanism. These electrons are emitted with large impact parameter with negligible momentum transfer from the projectile. With increase in the emission energy, it is observed

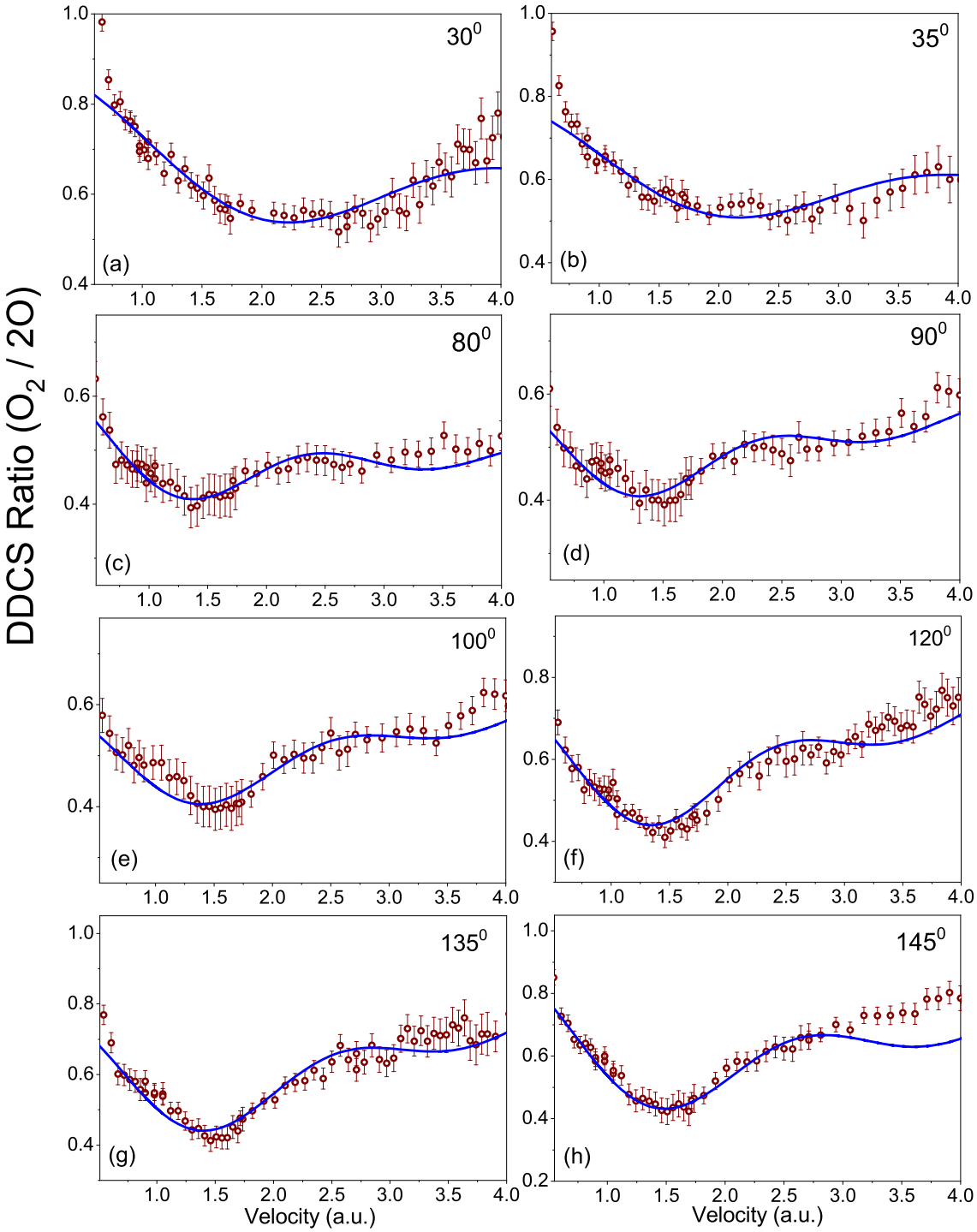

Figure 4.9: Experimental-to-theoretical DDCS ratios ($\frac{d^2\sigma_{O_2}}{d\Omega d\epsilon}/\frac{d^2\sigma_{2O}}{d\Omega d\epsilon}$) along with the blue solid lines showing the fitting in Equation 4.16.

that the cross section for extreme forward angles are slightly higher as compared to the extreme backward angles. For example, in case of 90 eV, the DDCS for forward angle (30^0) is higher than that for the backward angle (145^0) by a factor of 1.3. Similarly for 320 eV, this factor is about 1.8. This difference in DDCS is attributed by the forward-backward angular asymmetry. The peak like structure seen around 80^0 for high emission energies is due to the binary nature

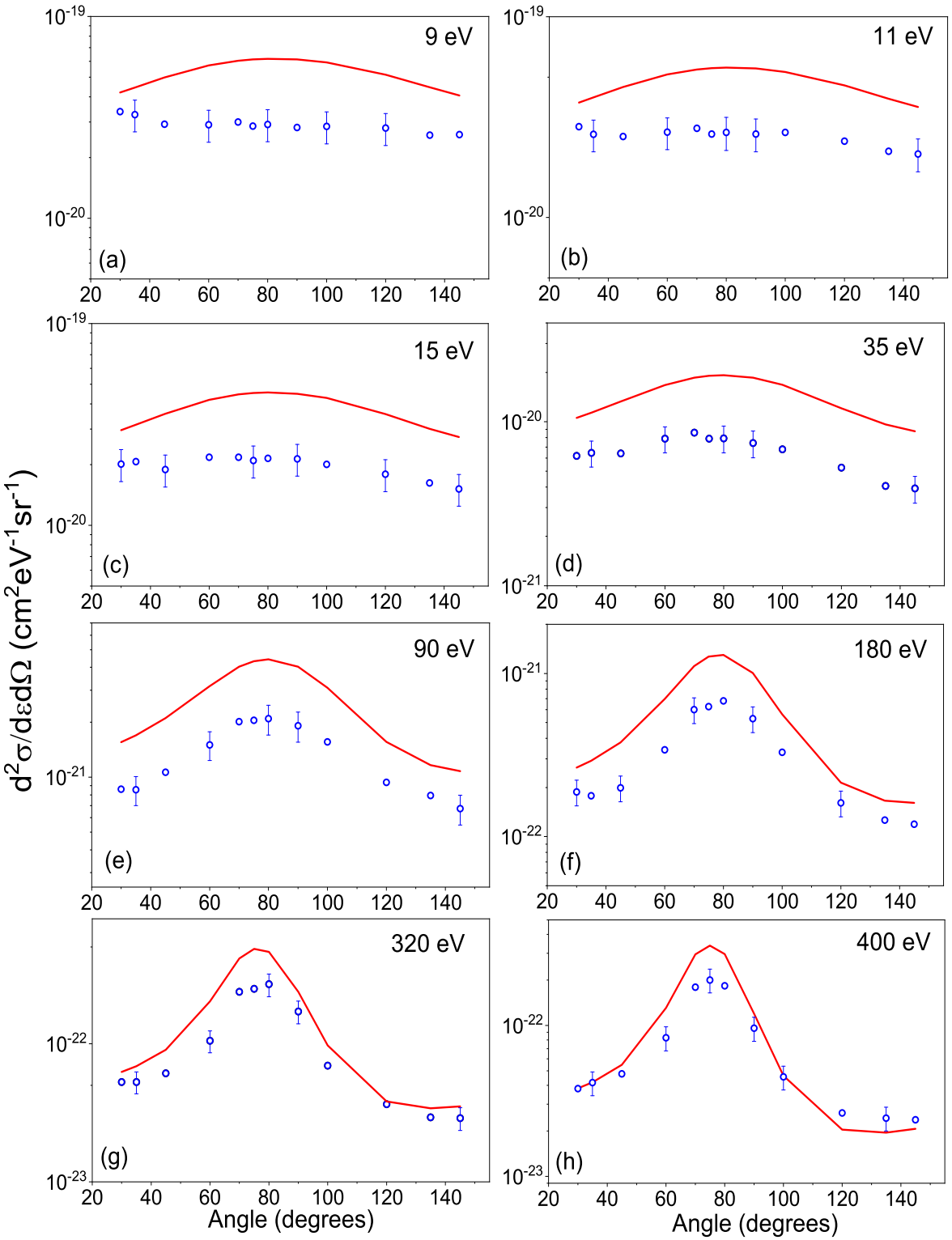

Figure 4.10: Collision system : 7 keV e^- + O_2, DDCS at different emission energies, solid line showing theoretical DDCS for 2O.

of collision, representing a violent collision between the projectile and target. The red solid line shows the theoretical calculations for twice of atomic oxygen. The calculated DDCS show a qualitative agreement with the measured data points and hence reveal all the different features

of collision mechanisms. However, quantitatively, it is seen that the DDCS for 2O are larger than the experimentally obtained DDCS for O_2 for all the different emission energies plotted in Figure 4.10. The discrepancy is seen to be maximum for the lowest electron energies.

4.4.4 Interference oscillations in O_2 from forward-backward asymmetry parameter (FBAP)

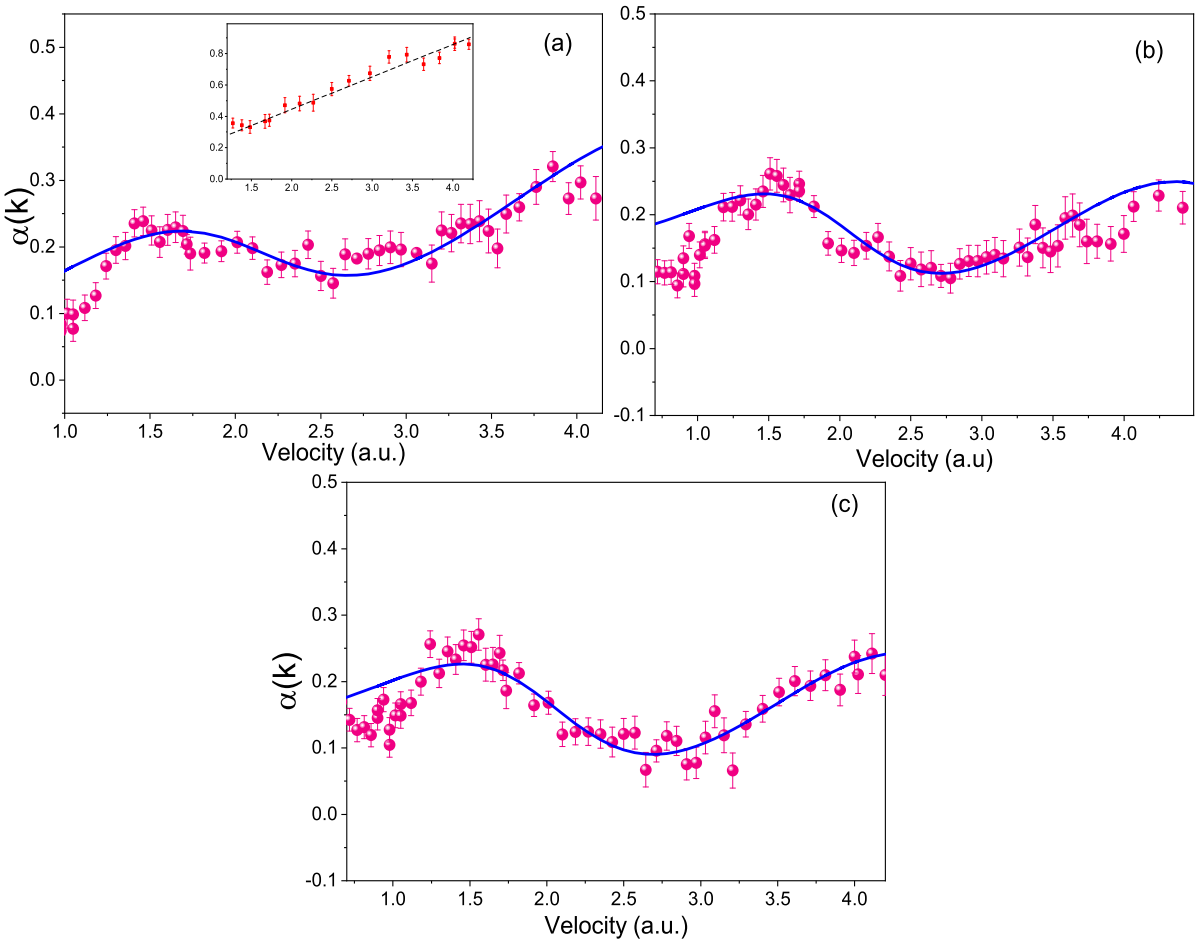

Figure 4.11: Forward-backward asymmetry parameter from measured DDCS for O_2 shown for (a) 45^0 and 135^0, (b) 35^0 and 145^0 and (c) 30^0 and 145^0. Solid line in each panel represents the model fitting given by Equation 4.20. Inset of (a) : Asymmetry parameter for atomic target, He using 45^0 and 135^0, black dashed line is for guide to eye.

Figure 4.11 displays the $\alpha(k,\theta)$ obtained from the measured DDCS for O_2 for different sets of forward and backward angles. In Figure 4.11(a), $\alpha(k,\theta)$ is derived using DDCS for 35^0 and its complementary angle 145^0, Figure 4.11(b) shows for 45^0 and 135^0. $\alpha(k,\theta)$ is plotted as a function of emitted electron velocity. A full sinusoidal oscillation is seen in both the Figure 4.11(a) and (b) within the ejected electron velocity range of 0.7 to 4.5 a.u. (in Figure 4.11(a)) and 1.0 to 4.2 a.u. (in Figure 4.11(b)). As already discussed above for N_2, the difference in frequency of oscillation between forward and backward angles generates the oscillation in $\alpha(k)$. Though in case of θ=35^0 (Figure 4.11(a)), the oscillation is observed about a

horizontal line around 0.16, but for θ=45^0 (Figure 4.11(b)), the oscillation is seen to vary between 0.06 and 0.3 with an increasing trend in the high velocity region. The entire experiment was performed with very good counting statistics, further ensuring that the oscillations in $\alpha(k)$ were not contributed due to statistical fluctuations. The inset of Figure 4.11(a) shows the variation of $\alpha(k)$ as a function of electron velocity for the atomic target, Helium. Here also $\alpha(k)$ is calculated for 35^0 and 145^0. The asymmetry parameter for helium is seen to increase monotonically with velocity. Such a monotonic behaviour is a well known and general phenomenon for ion-atom collisions [5]. The black dashed line in the inset is a guiding line to indicate the steady increase of the FBAP for He atom, in contrast to the oscillations seen for O_2 molecule. The asymmetry parameter for O_2 has been fitted with the model given in Equation 4.20. The fitted function is displayed by the blue solid lines in all the panels in Figure 4.11. The fitted curve is seen to have an overall good agreement with the calculated values of $\alpha(k)$, except for the very low velocity region. In this region, though a qualitative agreement is seen, but quantitatively, the fitting overestimates the derived values of $\alpha(k)$. The fitting parameter β, found to be 1.14 for θ=35^0 and 1.15 for θ=45^0 provided a good fitting to the asymmetry parameter.

Although in Figure 4.7 (for N_2) and Figure 4.11(a) and (b) we have shown the forward backward asymmetry parameter for complementary angles, like 35^0-145^0 and 45^0-135^0, however, this is not an absolute necessity. In Figure 4.11(c), $\alpha(k)$ has been derived for two non-complementary angles i.e. 30^0 and 145^0. In this case also a clear oscillatory structure is seen about a horizontal line in the velocity range of 0.7 to 4.2 a.u. The model fitting of Equation 4.20 (shown by blue solid line) is seen to match well beyond 1.25 a.u. The pattern of oscillation in Figure 4.11(c) looks similar to that observed in Figure 4.11(a) and (b). The evidence of oscillatory structure even between non-complementary angles arises due to the fact that the DDCS values for the low forward angles are almost similar (i.e., not much variation exists in the DDCS for angles near 35^0, as seen from Figure 4.10). Likewise, similar behaviour is also observed for the extreme backward angles. Hence, one low forward angle and a high backward angle can suffice for revealing the oscillation in asymmetry parameter.

4.5 Conclusions

In conclusion, we have shown the evidence of interference oscillations from the ionization channel for multi-electronic targets N_2 and O_2 when collided with 7 keV electrons. The experimental-to-theoretical DDCS ratios for N_2 and O_2 revealed clear oscillatory structures due to the Young type interference effect for all the emission angles. For atomic nitrogen and oxygen, theoretical DDCS values were used for determining the ratios, and hence it was observed that the shape of oscillation depended on the choice of effective charge. The forward-backward asymmetry parameter ($\alpha(k)$) which was obtained only by using the measured DDCS for the molecular targets, displayed clear signature of interference oscillations. In case of N_2,

periodic deviations were seen in the asymmetry parameter which indicated the presence of higher order scattering mechanism. However, such higher order effects were not observed for O_2 molecule. To make a comparative study of the variation of $\alpha(k)$ for molecular and atomic target, asymmetry parameter was also calculated for Helium, which showed a monotonically increasing behaviour. The remarkable results obtained from the present work provided an unambiguous evidence of the interference effect for multielectronic diatomic molecules N_2 and O_2 when probed with electrons.